Acta Materialia 177 (2019) 178–186

Contents lists available at ScienceDirect

Acta Materialia

journal homepage: www.elsevier.com/locate/actamat

Full length article

Effect of 60° dislocation on transformation stresses, nucleation, and growth for phase transformations between silicon I and silicon II under triaxial loading: Phase-field study

Hamed Babaei [a], Valery I. Levitas [b, c, *]

[a] Department of Aerospace Engineering, Iowa State University, Ames, IA, 50011, USA
[b] Departments of Aerospace Engineering and Mechanical Engineering, Iowa State University, Ames, IA, 50011, USA
[c] Ames Laboratory, Division of Materials Science and Engineering, Ames, IA, 50011, USA

ARTICLE INFO

Article history:
Received 7 May 2019
Received in revised form
10 July 2019
Accepted 15 July 2019
Available online 25 July 2019

Keywords:
Phase-field approach
Martensitic phase transformation
Lattice instability condition
Dislocation
Nanostructure

ABSTRACT

Stress-induced martensitic phase transformations (PTs) at a stationary 60° dislocation in single-crystalline Si are modeled by an advanced phase-field approach (PFA), which takes into account the lattice instability conditions obtained by atomistic simulations for the general stress tensor. Finite elastic, transformation, and plastic strains are considered. Finite element method (FEM) simulations elucidate two different mechanisms of nucleation and nanostructure evolution for two different stress-hysteresis cases. For a traditional finite-stress-hysteresis region, the PT starts with the barrierless nucleation of a thermodynamically-equilibrium-incomplete embryo, which loses its stability and grows forming a propagating martensitic band with distinct interfaces. However, in the unique zero-stress-hysteresis region, where PT for defect-free crystal occurs homogeneously through intermediate phases without nucleation, interfaces, and growth, the PT starts at a dislocation but spreads quasi-homogeneously, without interfaces, similar to the defect-free case; the macroscopic stress-strain curve is horizontal and without hysteresis during direct-reverse PTs. Despite large normal stresses produced by dislocation in the range of $\pm(6-12)$ GPa, a relatively small reduction in macroscopic PT stress by 1.6 GPa is quantitatively explained by mutually compensating contributions of stresses into lattice instability criterion.

1. Introduction

It is well-accepted that nucleation during martensitic phase transformations (PTs) initiates at stress concentrators caused by dislocations; see analytical models in Refs. [1–4], review [5], and PFA simulations [6–10]. Within PFA, stress concentration at dislocations causes barrierless nucleation of martensite at temperatures above the lattice instability temperature and stresses below the lattice instability stresses for an ideal (defect-free) crystal. However, quantitative information on how different dislocation configurations reduce transformation stresses for different PTs is still lacking, especially for stress-induced PTs.

Monocrystalline silicon (Si) is one of the most important materials in the semiconductor industry, especially in the micro/nano-electromechanical systems (MEMS/NEMS). To design and fabricate MEMS/NEMS devices, a thorough understanding of PTs in Si, as an inelastic deformation mechanism, is essential. The lattice instability (i.e. PT initiation) conditions for stress-induced martensitic cubic-to-tetragonal Si-I↔Si-II PTs in ideal (defect-free) crystal under general tensorial stress states were recently obtained using theoretical predictions within PFA followed by molecular dynamics (MD) and density functional theory (DFT) validation and specification [11–14]. Without shear stresses, the conditions for direct and reverse PTs were described in 3D space σ_i (normal-to-cubic-faces stresses) by two intersecting planes, which coincide after intersection (see Fig. 1 for $\sigma_1 = \sigma_2$). Thus, there are two different regions of instability: first, a finite-stress-hysteresis region, and second, an unusual zero-stress-hysteresis region.

Within the zero-stress-hysteresis region, the traditional nucleation and two-phase growth is substituted by homogeneous and hysteresis-free first-order PTs, as observed in MD [12] and PFA [15] simulations. During the homogeneous transformation, the system passes through an infinite number (continuum) of intermediate crystal lattices (phases), which are in indifferent thermodynamic equilibrium and can be arrested and studied by fixing the strain in

* Corresponding author. Departments of Aerospace Engineering and Mechanical Engineering, Iowa State University, Ames, IA, 50011, USA.
E-mail address: vlevitas@iastate.edu (V.I. Levitas).

https://doi.org/10.1016/j.actamat.2019.07.021
1359-6454/

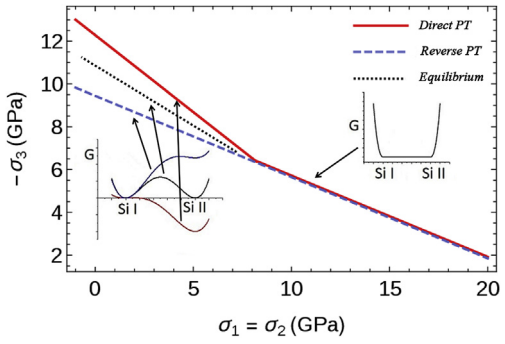

Fig. 1. Crystal lattice instability stress lines in the stress plane for direct and reverse phase transformations in Si. σ_3 is uniaxial compressive stress and $\sigma_1 = \sigma_2$ are lateral biaxial tensile stresses. Two characteristic regions are present: with finite stress hysteresis for $\sigma_1 = \sigma_2 \leq 8.41$ GPa and with zero stress hysteresis for $\sigma_1 = \sigma_2 > 8.41$ GPa. A schematic plot of the Gibbs energy versus order parameter for the fixed stress tensor is shown for each instability line (corresponding to the disappearance of the energy minimum) and phase equilibrium line (corresponding to the equal energy minima for both phases). For the zero-stress-hysteresis region, the energy barrier between phases transforms to a plateau corresponding to a continuum of intermediate homogeneous phases, which are in indifferent thermodynamic equilibrium. In this region, Si-I↔Si-II PTs occur homogeneously (i.e. without nucleation and growth), without hysteresis, dissipation, internal stresses and corresponding damage.

one direction. Homogeneous transformation and zero hysteresis are the most favorable features for various PT-related applications reducing energy dissipation and damage due to internal stresses caused by transformation strain.

The PFA model for Si-I↔Si-II PTs in ideal crystal under a general stress tensor, which is calibrated by atomistic simulations [11,15] allows us to quantitatively study the effect of defects on martensitic PTs. Si-I→Si-II PTs are of special interest because they are accompanied by very large anisotropic transformation strain, which in MD simulations [12,13] is accommodated elastically (i.e. without dislocations and twinning), thus generating large internal stresses.

The presence of the unusual zero-stress-hysteresis region also raises two crucial questions:

- With the heterogeneity of the internal stresses produced by dislocations, will a quasi-homogeneous evolution of martensitic nanostructure still be possible?
- How do dislocations affect the macroscopic stress hysteresis, i.e. may they lead to a non-zero macroscopic hysteresis despite being within the local zero-stress-hysteresis region?

Moreover, numerous previous studies have shown that under hydrostatic loading there is a significant difference between the instability pressure obtained by atomistic simulations, specially 64-80 GPa for Si-I→Si-II PT [14,16,17] and those obtained by experiment, e.g. 10-12 GPa [19]. However, the experimental works [18–20] for non-hydrostatic uniaxial/multiaxial loadings using nanoindentation or diamond-anvil cell on real (defective) crystals reveal that the PT stress is in the same range as in atomistic simulations for ideal (defect-free) crystals [14], specially $\sim$ 11 GPa. Thus, studies must be performed to determine why the effect of dislocations on uniaxial/multiaxial non-hydrostatic instability stresses is relatively small.

In this work, we utilize our PFA model [11,15] to study Si-I→Si-II PT at a single stationary 60° mixed perfect dislocation within monocrystalline Si using FEM. We investigate the effect of dislocation on the nucleation of Si II and nanostructure evolution for finite- and zero-stress-hysteresis regions. Furthermore, we quantitatively explain why dislocation has a small effect on the instability stresses for non-hydrostatic loadings. Obtained results represent a closure of the multiscale problem of predicting the PT initiation conditions for real (defective) materials starting with atomistic simulations, development of PFA for an ideal crystal, and solving PFA problems for a crystal with defect.

Generally, due to high applied and internal stresses, various other processes may occur, such as motion of the initial dislocation and generation and motion of new dislocations and cracks. To study all these processes, corresponding complex theory of interaction between PT, plasticity, and fracture should be developed, see e.g., a simplified theory in Refs. [9,10] and references there for coupled PT and plasticity. This will require significant time for development and much longer computational time. Still, since many of parameters of this theory will be unknown, results will have significant indeterminacy. That is why our approach using single static dislocation (such as in classical problem formulation [1–3,5–7]) and neglecting nucleation of new dislocations and cracks is much more realistic, economic, and focused, and it allows us to answer questions that we formulated. MD simulations of the Si-I→Si-II PT under the same stresses but without initial dislocation [12,13] did not show nucleation of new dislocations or cracks. Immobility of an initial dislocation can be justified by assumptions of the high Peierls barrier and much lower mobility of the dislocation than mobility of the phase interface, which, however, currently do not have any confirmations or contradictions with experiment or MD simulations.

We designate vectors and tensors with boldface symbols and designate contractions of tensors $\boldsymbol{A} = \{A_{ij}\}$ and $\boldsymbol{B} = \{B_{lk}\}$ over one and two indices as $\boldsymbol{A} \cdot \boldsymbol{B} = \{A_{ij} B_{jk}\}$ and $\boldsymbol{A} : \boldsymbol{B} = A_{ij} B_{ji}$ respectively. The transpose of $\boldsymbol{A}$ is $\boldsymbol{A}^T$, and I is the unit tensor; symbol $\forall$ means "for all"; $:=$ means equal by definition; and ∇ and ∇_0 are the gradient operators with respect to the deformed and undeformed states.

2. Model and lattice instability conditions

The formulations in this work are based on the general PFA developed in Ref. [11], which was specified for cubic-to-tetragonal Si I↔Si II PTs in Ref. [15]. Here, we slightly advance the kinematics by taking into account the plastic deformation due to a single static dislocation. The complete system of equations is presented in the Appendix. Here we will discuss the specific lattice instability conditions for defect-free Si I and Si II.

The lattice instability or PT initiation conditions for cubic-to-tetragonal Si I↔Si II PTs were obtained via MD simulations for various combinations of all six components of the Cauchy stress tensor in Refs. [12,13]. We consider loading by three components of the Cauchy (true) stresses σ_i normal to the cubic faces in the deformed state. In 3D stress σ_i space, all points for direct and reverse instability stresses have been located close to two planes that coincide after intersection:

$$\begin{aligned} A\rightarrow M: &\quad \begin{cases} \sigma_{ef}^{f} := 0.36(\sigma_1+\sigma_2) - \sigma_3 \geq 12.29 \text{ GPa} \quad \textit{if} \quad -\sigma_3 \geq 6.23 \text{ GPa} \\ \sigma_{ef}^{0} := 0.19(\sigma_1+\sigma_2) - \sigma_3 \geq 9.45 \text{ GPa} \quad \textit{otherwise} \end{cases} \\ M\rightarrow A: &\quad 0.19(\sigma_1+\sigma_2) - \sigma_3 \leq 9.45 \text{ GPa}. \end{aligned} \tag{1}$$

Here, the effective instability stress for the finite-stress-hysteresis region σ^f_{ef} and for the zero-stress-hysteresis region σ^0_{ef} are introduced. For equal stresses in two lateral directions ($\sigma_1 = \sigma_2$), the instability conditions are shown in 2D stress plane in Fig. 1.

It can be observed that increasing the lateral tensile stresses reduces not only instability stresses for the direct and reverse PT, but also their difference (i.e. the stress hysteresis), all the way down to the intersection point. From there on, the two instability lines coincide and the stress hysteresis vanishes. We will discuss transformation behavior separately for lateral stresses in the finite-stress-hysteresis region as well as the zero-stress-hysteresis region.

3. Crystal and dislocation structures

Silicon as a covalent bonded material crystallizes in a diamond cubic structure with tetrahedrally coordinated atoms [21]. The lattice parameter a is 0.543 nm at room temperature. The crystal structure consists of two interpenetrating fcc lattices with one atom at (0,0,0) and another one at (1/4,1/4,1/4). The structure has two types of {111} most closely packed atomic planes, i.e. a widely spaced set termed the *shuffle-set* with a spacing of $\frac{\sqrt{3}}{4}a$ between the adjacent planes and a narrowly spaced one termed *glide set* with a spacing of $\frac{\sqrt{3}}{12}a$ [22].

Dislocations in diamond cubic structure crystals are energetically stable when they lie parallel to the ⟨110⟩ directions on the {111} slip planes due to high Peierls potential. Therefore, a stable dislocation loop has a hexagonal shape with two opposite screw segments and four 60° segments. Besides, a glissile dislocation has the smallest Burgers vector $\boldsymbol{b} = a/2\langle\bar{1}10\rangle$ on the {111} planes. The movement of such a dislocation occurs on planes located between widely or closely spaced atomic planes, namely shuffle-set or glide-set, respectively. Geometrically, a dislocation on a glide-set plane is dissociated into two Shockley partial dislocations bounding a strip of intrinsic stacking fault. However, a dislocation in the shuffle-set plane is perfect because there is no stable stacking fault on the shuffle planes. From numerous published reports on observations of dislocation structures, it is now commonly believed that such dislocations are dissociated at high temperatures while they are perfect at low temperatures. Besides, some theoretical studies with *ab initio* calculation have shown that a perfect shuffle-set dislocation is favorable under high stress [23,24] because the activation energy for the nucleation of a shuffle-set dislocation is much lower than that of a glide-set one under stresses above 4 GPa [24]. Therefore, because our simulations are performed for high stress and low temperatures, we consider a 60° perfect shuffle-set dislocation.

4. Problem formulation and computational approach

We now consider some examples showing the effect of a single 60° dislocation on martensitic nanostructure evolution and instability stresses for different loading conditions. The coupled system of mechanics and the Ginzburg-Landau equation Eqs. 2–18 have been solved simultaneously using the FEM. We have developed a large strain FEM-based code in the deal.II program library framework [25]. The governing PFA and mechanics equations are solved iteratively in a decoupled manner using the Newton's method. We have used the quadratic quadrilateral elements for spatial discretization of both the mechanics and phase field equations and a Crank-Nicolson finite difference scheme for time discretization of the Ginzburg-Landau equation. The three-dimensional and fully geometrically-nonlinear response of an anisotropic crystal has been modeled. Although the computations are carried out in the reference configuration, the results are presented in the current configuration. The following material parameters are used [26,27]: components of transformation deformation gradient $U^1_t = U^2_t = 1.1753$ and $U^3_t = 0.553$; kinetic coefficient $L = 2600\ (\text{Pa.s})^{-1}$; gradient coefficient $\beta = 2.59 \times 10^{-10}$ N; elastic constants of Si I $C^{11}_0 = C^{22}_0 = C^{33}_0 = 167.5$ GPa, $C^{44}_0 = C^{55}_0 = C^{66}_0 = 80.1$ GPa, $C^{12}_0 = C^{13}_0 = C^{23}_0 = 65.0$ GPa, and elastic constants of Si II $C^{11}_1 = C^{22}_1 = 174.76$ GPa, $C^{33}_1 = 136.68$ GPa, $C^{44}_1 = C^{55}_1 = 60.24$ GPa, $C^{66}_1 = 42.22$ GPa, $C^{12}_1 = 102$ GPa, $C^{13}_1 = C^{23}_1 = 68$ GPa.

A 3D sample of size $40 \times 20 \times 20\text{nm}^3$ is considered. A schematic of the sample including a single 60° dislocation is depicted in Fig. 2. The dislocation line (the purple line) lying within the (111) slip plane starts from a point at the center of the front face and ends at a point on the bottom face, making a 60° angle with the slip direction $[\bar{1}10]$ (the red arrow). The dislocation is modeled through applying the plastic simple shear strain $\gamma = \frac{|\boldsymbol{b}|}{H}$ within a triangular dislocation band (green area) in the Burgers vector $\boldsymbol{b} = \frac{a}{2}[\bar{1}10]$ direction. The dislocation band is the space between two triangular planes parallel to the slip plane (111) with the distance of the dislocation height H. The lattice parameter a for Si is 0.543 nm and the dislocation height H is considered equal to the doubled (111) interplanar distance, i.e. $H = 2 \times 0.235 = 0.47$ nm; therefore, the plastic shear $\gamma = \frac{\sqrt{2}a}{2H} = 0.817$.

In addition to Eq. (18) as the boundary condition for the order parameter, the following boundary conditions are used for the mechanical problem. A point at the corner, where the origin of the coordinate system is located, is fixed for all displacement components. The bottom face, the left face and the back face are fixed for normal-to-the-face displacement and free of shear stresses. Thus, these faces are symmetry planes and our simulation domain is one-eighth of the actual sample, being symmetric in all three directions. The right face and front face are either free or under fixed homogeneous tensile normal Cauchy stresses $\sigma_1 = \sigma_2$. The top face is either under prescribed normal compressive stress σ_3 for stress-controlled loading or under compressive displacement for strain-controlled loading; for both cases, shear stresses at these faces are zero. As the initial conditions for order parameter, we consider perturbations of $\eta = 0.01$ everywhere, since without perturbations the driving force for the evolution of the order parameter is zero.

5. Nanostructure evolution around a dislocation for different hysteresis cases

In this section, we study how the presence of a dislocation affects martensitic PTs in single crystal silicon: PT stresses, nanostructure evolution, and a novel zero-stress-hysteresis phenomenon. It was thoroughly studied in Ref. [15] how the entire

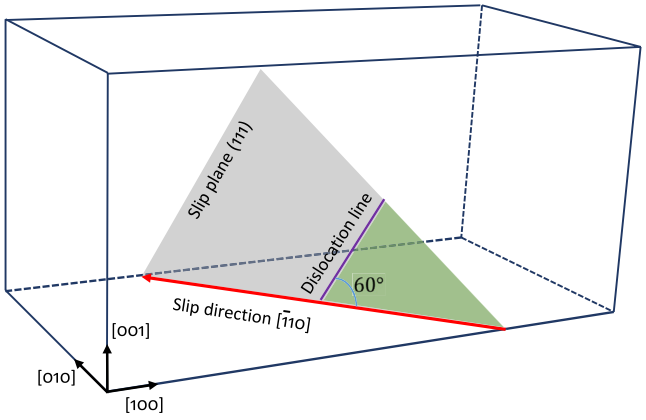

Fig. 2. Schematics of the sample with a 60° dislocation.

Si-I↔Si-II PT process and nanostructure evolution in defect-free single crystal are affected by the stress state. In the finite-stress-hysteresis region (e.g. for $\sigma_1 = \sigma_2 = 0$), the PT evolution process includes the nucleation of martensite leading to the formation of martensitic bands with distinct interfaces which propagate until PT completion in the entire sample. As the tensile lateral stresses increase (e.g. $\sigma_1 = \sigma_2 = 5$ GPa), reducing the stress hysteresis, the interface width increases and the interfaces are not as plain and distinct as for higher hysteresis. Finally, in the zero-stress-hysteresis region, despite the heterogeneous initial perturbation for the order parameter, the system undergoes a homogeneous and hysteresis-free first-order PT without nucleation, formation of martensitic bands and their following growth.

Here, we consider PT for a sample with a static 60° dislocation in the finite-stress-hysteresis region and zero-stress-hysteresis region separately.

First, let us consider a loading for the finite-stress-hysteresis region. A uniaxial compressive stress $\sigma_3 = -12$ GPa is applied in the vertical direction [001] with no applied stress in the lateral directions [100] and [010], namely $\sigma_1 = \sigma_2 = 0$. This compressive stress is slightly less than the direct instability stress 12.29 GPa for uniaxial loading. Although we have not reached the instability stress for a defect-free case, the stress concentration around the dislocation line is sufficient to satisfy the instability condition and turn the dislocation line to a nucleation site. Fig. 3 shows that an embryo is formed around the dislocation line. While the embryo of the intermediate phase with $\eta \sim 0.5$ around the dislocation grows, the order parameter within the embryo increases so that the embryo finally turns to an inclined martensitic band within the sample. The martensitic band then propagates, reaches other external faces and transforms the sample into martensite.

A completely different mechanism governs the onset of the PT for the loading within the zero-stress-hysteresis region, in particular, for $\sigma_1 = \sigma_2 = 10$ GPa and $\sigma_3 = -5.5$ GPa. We again apply the compressive stress σ_3 slightly below the instability stress for the corresponding lateral stresses, being 5.65 GPa. It can be seen in Fig. 4 that PT starts in the close vicinity of the dislocation line, where the internal dislocation stress field adds up to the external applied stresses and exceeds the instability stress. Then PT spreads toward the regions where the dislocation stress field is favorable for such a transformation strain. Next, the intermediate phase keeps propagating into the entire sample without forming a distinct interface and transforms the sample into a relatively homogeneous intermediate phase with $\eta = 0.5$ at $t = 1.6$ ps. From then on, the entire system almost homogeneously transforms to the product phase, passing through all intermediate homogeneous phases. Therefore, it can be concluded that, when the stress state lies within the zero-stress-hysteresis region, despite the heterogeneity of the internal stresses produced by dislocations, a quasi-homogeneous PT still occurs.

To check whether the zero-stress-hysteresis obtained for a defect-free sample is obtainable for a sample with a dislocation, a compressive strain-controlled loading in the third direction with lateral stresses $\sigma_1 = \sigma_2 = 10$ GPa is applied on the sample with a dislocation. The global stress σ_3 averaged over the top face is plotted against the Lagrangian strain in Fig. 5 for a cyclic direct and reverse PT. The dots in the figure show the direct and reverse instability stress being 5.65 GPa for such a loading condition. It can be seen that, even with dislocation, the stress hysteresis is zero and the heterogeneous internal stresses around the dislocation do not produce hysteresis.

6. Effect of dislocation on the instability stress

Several simulations were conducted applying uniaxial compressive stresses below the instability stress $\sigma_3 = -12.29$ GPa for a defect-free sample. For the stresses below 10.7 GPa, a stable martensitic embryo of a intermediate phase is formed near the dislocation, which could not grow. Stress $\sigma_3 = -10.7$ GPa is the lowest uniaxial stress, for which the embryo loses its stability and grows to the completion of PT in the entire sample with the same nanostructure evolution as shown in Fig. 3 for $\sigma_3 = -12$ GPa. Thus, a single dislocation reduces the transformation stress by 1.59 GPa compared to that for a defect-free Si.

To understand the quantitative and qualitative effect of the dislocation on the instability stress, the distribution of the internal stresses produced by dislocation should be analyzed. Therefore, the field of all three normal components of the dislocation stress are shown in Fig. 6 within the $(01\bar{1})$ plane, which cuts the sample into two equal parts. From here on, we designate the internal stresses produced by dislocation with $\tilde{\sigma}$. In addition, the figures include plots showing the distribution of the corresponding stress along the designated lines, which represent the symmetry axes for each stress distribution.

Two main points should be noted in these figures. First, while $\tilde{\sigma}_1$ and $\tilde{\sigma}_3$ have the same symmetry line [122], the $\tilde{\sigma}_2$ symmetry line, [522], is different. This is important because the shape of the stress fields and the direction in which they have the maximum value determine the direction along which the embryo and the following martensitic band are formed. Second, the regions of maximum tensile $\tilde{\sigma}_1$ and $\tilde{\sigma}_2$ are at the opposite side of the region of maximum compressive $\tilde{\sigma}_3$. It means that, although there are considerable internal stresses around the dislocation line, reaching approximately 10, 12, and 6 GPa for $\tilde{\sigma}_1$, $\tilde{\sigma}_2$ and $\tilde{\sigma}_3$, respectively, they are "out of phase" and reduce each other's promoting effect.

To quantitatively understand the reason why the dislocation does not reduce the instability stress significantly and only by 1.6 GPa, the fields of the effective instability internal stress from dislocation $\tilde{\sigma}^f_{ef} = 0.36(\tilde{\sigma}_1 + \tilde{\sigma}_2) - \tilde{\sigma}_3$ for the finite-stress-hysteresis region and $\tilde{\sigma}^0_{ef} = 0.19(\tilde{\sigma}_1 + \tilde{\sigma}_2) - \tilde{\sigma}_3$ for the zero-stress-hysteresis

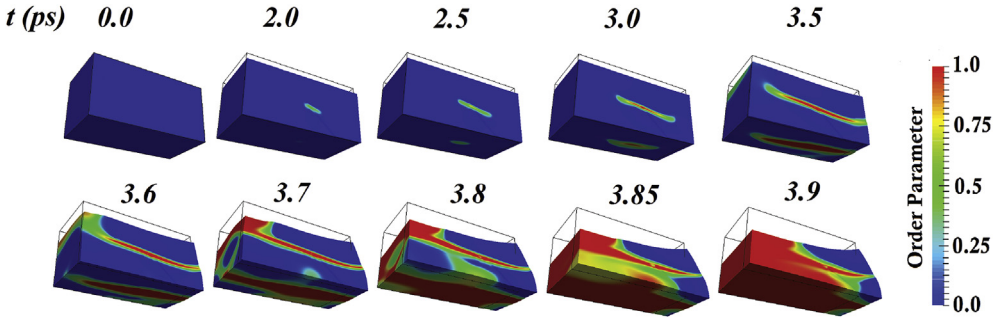

Fig. 3. Evolution of martensitic nanostructure during Si-I↔Si-II PT for uniaxial compressive stress $\sigma_3 = -12$ GPa at $\sigma_1 = \sigma_2 = 0$, i.e. in finite-stress-hysteresis region.

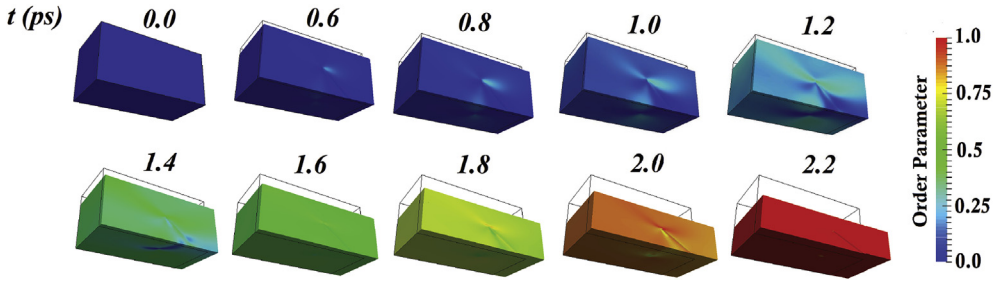

Fig. 4. Evolution of martensitic nanostructure during Si-I↔Si-II PT for uniaxial compressive stress $\sigma_3 = -5.5$ GPa and tensile lateral stresses $\sigma_1 = \sigma_2 = 10$ GPa, i.e. in the zero-stress-hysteresis region.

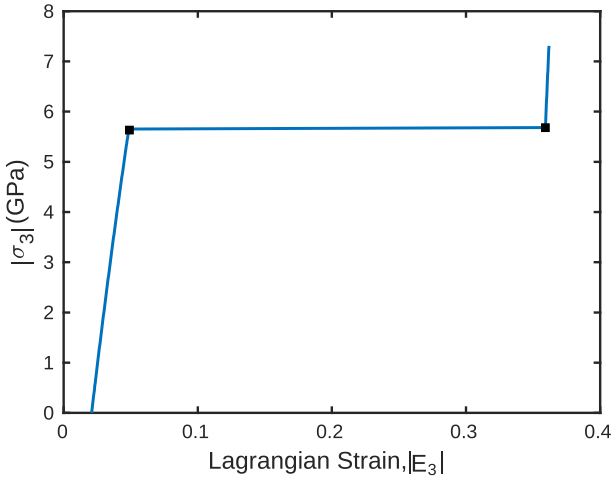

Fig. 5. Stress-strain curve for a strain-controlled loading of a sample with dislocation in the third direction [001] and lateral tensile stresses $\sigma_1 = \sigma_2 =$ 10 GPa, which demonstrates zero hysteresis. Dots shows the direct and reverse instability stresses.

region (that contribute to the instability condition (2)) are plotted in Fig. 7. These figures illustrate the promoting and suppressing regions for PT initiation, which in turn clarifies where and in which direction nucleation and propagation of the martensite will occur. The same distributions are shown along the designated line $[\bar{1}11]$, one of the promoting PT stress branches. It can be seen in Fig. 7 that $\tilde{\sigma}^f_{ef}$ forms a triple rosette of PT-promoting regions (red) along with twofold PT-suppressing regions (blue) in between. For $\tilde{\sigma}^0_{ef}$, one more PT-suppressing branch above the dislocation core is observed, covering an even broader zone than the two lower suppressing zones. Note that blue PT-suppressing regions for direct PT are PT-promoting regions for the reverse PT in Si II. Also, the promoting effective instability stresses $\tilde{\sigma}^f_{ef}$ and $\tilde{\sigma}^0_{ef}$ have maximum values of 3 GPa and 1.7 GPa, respectively, close to the dislocation core, which decrease with distance from the dislocation core.

The differences between finite- and zero-stress-hysteresis cases can be explained if we notice that $\tilde{\sigma}_1$ and $\tilde{\sigma}_2$ contribute to the effective instability stress $\tilde{\sigma}^0_{ef}$ with a lower weight, specifically 0.19 compared to $\tilde{\sigma}^f_{ef}$, specifically 0.36.

To gain further insight into the nucleation process, we plot the total effective stress (produced by external stress plus dislocation stress) $\sigma^f_{ef} - 12.29$ and stationary solutions for embryos along the line $[\bar{1}11]$ in Figs. 8 and 9 for a different uniaxial external compressive stress σ_3. For σ_3, slightly below −9.5 GPa, the instability condition $\sigma^f_{ef} \geq 12.29$ GPa is not satisfied for all material points. Once $|\sigma_3|$ reaches 9.5 GPa, the instability condition is met in a tiny region around the dislocation core and a very small embryo appears. With increasing $|\sigma_3|$ up to 10.69 GPa, the region in which the instability condition is satisfied increases along with the size of equilibrium embryo and maximum η within. Note that the size of the embryo significantly exceeds the size of the region where the instability condition is met, because it is determined by thermodynamic equilibrium rather than instability conditions. When $|\sigma_3|$ increases to 10.7 GPa, the Si II embryo loses its stability and grows to complete PT in the major part of the sample. Note that an embryo that loses its stability is not a critical nucleus in the classical theory of nucleation. A classical critical nucleus corresponds to the maximum of the Gibbs free energy vs. size, i.e., nuclei of all sizes are unstable. In our case, embryos of all sizes below some size are in a stable thermodynamic equilibrium and correspond to the minimum of energy, which disappears at some size. This nucleus can be called the *largest equilibrium nucleus*. Note that the maximum order parameter in the largest equilibrium nucleus is below 0.3, i.e. very

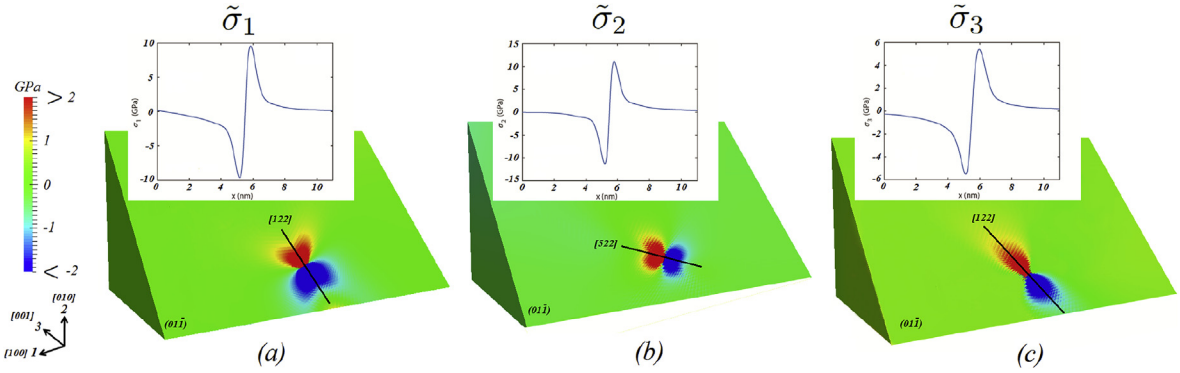

Fig. 6. Fields of internal stresses $\tilde{\sigma}_1$, $\tilde{\sigma}_2$, and $\tilde{\sigma}_3$ around the dislocation line within the $(01\bar{1})$ plane, which cuts the sample into two equal parts. In addition, the distribution of the corresponding stress along the designated lines, which represent symmetry axes for each stress distribution, is shown.

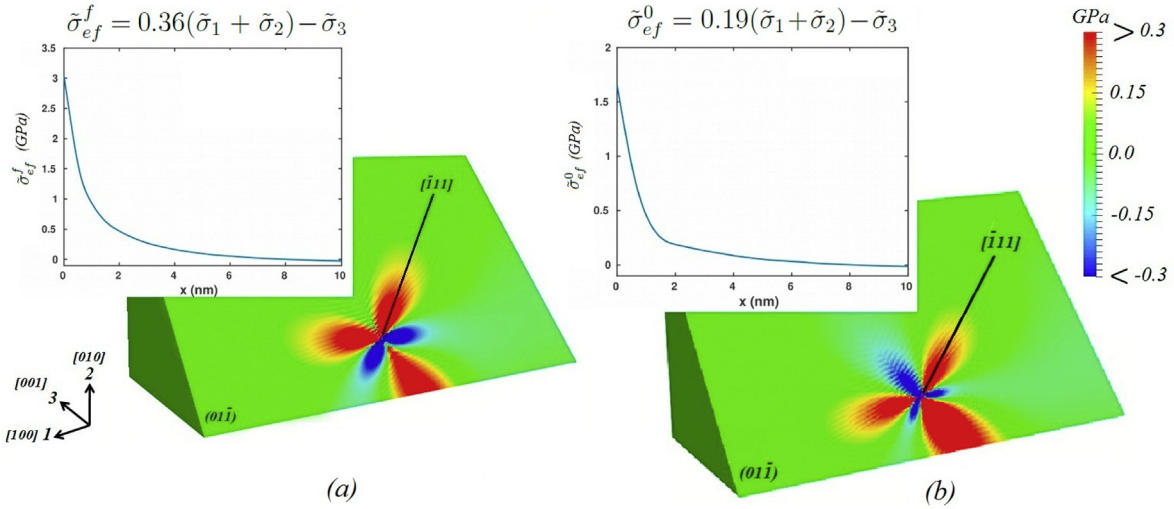

Fig. 7. Fields of the effective instability stress $\tilde{\sigma}^f_{ef} = 0.36(\tilde{\sigma}_1 + \tilde{\sigma}_2) - \tilde{\sigma}_3$ (a) and $\tilde{\sigma}^0_{ef} = 0.19(\tilde{\sigma}_1 + \tilde{\sigma}_2) - \tilde{\sigma}_3$ (b) around the dislocation line within the $(01\bar{1})$ plane, which cuts the sample into two equal parts. In addition, the same distributions are shown along the designated line $[\bar{1}11]$, one of the promoting PT stress branches.

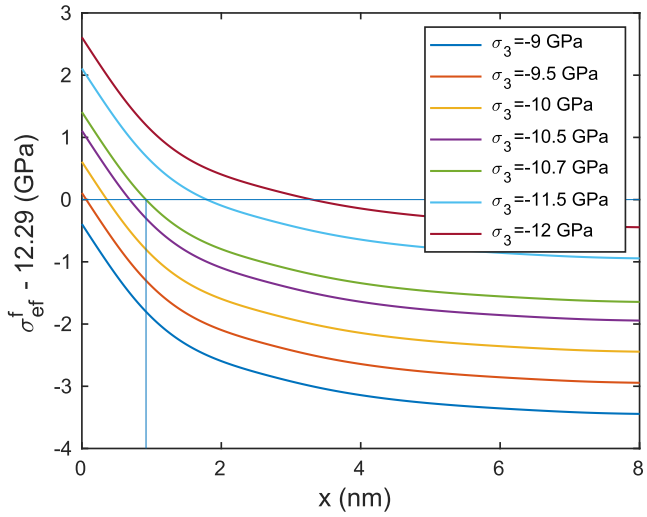

Fig. 8. Plot of $\sigma^f_{ef} - 12.29$ along the line $[\bar{1}11]$, starting from the dislocation core for different values of uniaxial external compressive stress σ_3.

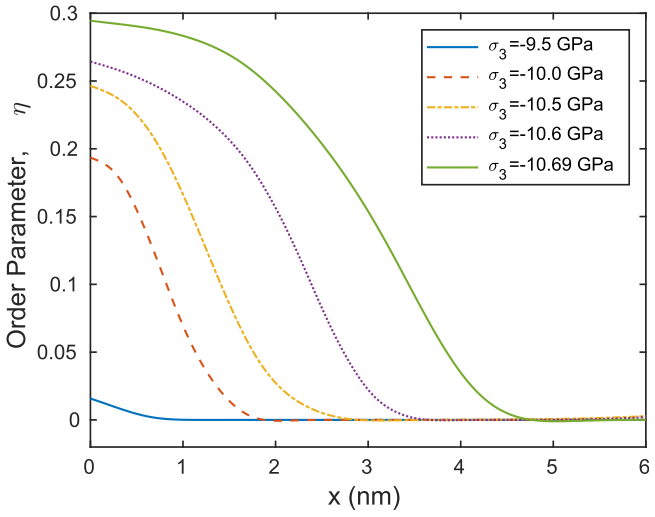

Fig. 9. Stationary solution for the order parameter characterizing an equilibrium embryo along the line $[\bar{1}11]$, starting from the dislocation core for different values of uniaxial external compressive stress σ_3.

far from the Si II. Application of the sharp interface approach, which operates with the complete nucleus of the product phase, should lead to significant inaccuracy.

Note that no embryo is formed along the lower red branch in Fig. 7 for the finite-hysteresis-region, which is surrounded by two PT-suppressing stress branches, even at $|\sigma_3| = 12GPa$ in Fig. 3. This may be because of closeness to the bottom boundary and internal stresses due to embryos that appeared earlier in the upper PT-promoting branches. Thus, exceeding of the instability conditions in some regions does not guarantee that PT will occur in this region because of the effect of processes at other locations.

To summarize, for uniaxial loading, the instability stresses for direct and reverse Si-I↔Si-II PTs in defect-free crystal are 12.29 and 9.45 GPa, respectively. Since it is not trivial to estimate the phase equilibrium stress, which depends on the interface orientation rather than only on σ_3, we estimate it as the semisum of the instability stresses, i.e. 10.87 GPa. Single dislocation produces a maximum effective instability stress $\tilde{\sigma}^f_{ef}$ of 3 GPa for Si-I→Si-II PT, and assuming approximate additivity of stresses, the Si I embryo should appear slightly above 9.29 GPa. However, it appears at 9.5 GPa, and the small difference is because of the small geometric nonlinearity before PT starts. Stress σ_3 must be increased to 10.7 GPa for the equilibrium embryo to reach the size of the largest equilibrium nucleus, which loses its stability and transform the entire sample in Si II. Thus, 10.7 GPa can be called the lattice instability stress in the presence of single dislocation, and it is less than our estimate for the phase equilibrium stress.

7. Conclusion

In this paper, stress-induced martensitic Si-I↔Si-II PTs at a stationary 60° shuffle-set dislocation in monocrystal is modeled by an advanced PFA developed in Ref. [11]. The key point in this approach is that, in contrast to previous approaches, it includes the lattice instability (i.e. PT initiation) conditions under a general stress tensor, which are calibrated by MD simulations for the same PTs under various combinations of normal-to-cubic-faces stresses

σ_1, σ_2, and σ_3 [12,13,15]. This, in particular, introduces a new zero-stress-hysteresis regime, which was found in Ref. [12] only for ideal crystal and was never studied for crystal with defects. Also, the model and simulations are based on a fully geometrically-nonlinear formulation for the general case of finite elastic, plastic and transformational strains, as well as anisotropic and different elastic properties of parent and product phases. In particular, the transformation strains for Si-I↔Si-II PTs are very large.

FEM simulations elucidate two different mechanisms of nucleation and nanostructure evolution for two different stress-hysteresis cases. For the traditional finite-stress-hysteresis region, the PT starts with the barrierless nucleation of a thermodynamically-equilibrium-incomplete embryo, which loses its stability and grows forming a propagating martensitic band with distinct interfaces. Dislocation generates three normal stresses in the range of $\pm(6-12)$ GPa; therefore, a large reduction in transformation stress due to dislocation is expected, which is not the case in experiments. However, our simulations showed a relatively small reduction in macroscopic PT stress by 1.6 GPa (i.e. from $\sigma_3 = -12.3$ to -10.7 GPa, in good correspondence with experiments), which is quantitatively explained by mutually compensating contributions of stresses to the lattice instability criterion. the first fulfillment of the instability criterion occurs at $\sigma_3 = -9.5$ GPa. In the range of σ_3 from -9.5 to -10.7 GPa a thermodynamically-equilibrium-incomplete embryo grows so that its size, as well as the maximum η within it, increases. Slightly below $|\sigma_3| = 10.7$ GPa, the largest equilibrium nucleus is formed, loses its stability, and grows at $\sigma_3 = -10.7$ GPa. The maximum order parameter in the largest equilibrium nucleus is below 0.3, i.e. very far from the Si II. Application of the sharp interface approach which operates with the complete nucleus of the product phase, should lead to significant inaccuracy.

In the unique zero-stress-hysteresis region, when PT for defect-free crystal occurs homogeneously through intermediate phases without nucleation, interfaces, and growth, the PT starts at a dislocation but spreads quasi-homogeneously, without interfaces, similar to the defect-free case. The macroscopic stress-strain curve for strain-controlled loading is horizontal and without hysteresis during direct-reverse PT. Thus, single dislocation does not spoil the ideal PT properties of a material in the zero-stress-hysteresis region.

Si-I→Si-II PT occurs at stresses on the order of 10 GPa and Si II cannot be retained at normal pressure to perform TEM study. That is why there is no experimental study of nucleation of Si II at dislocations. This makes theoretical and computational studies even more valuable.

All problems solved here with PFA could be solved as well with MD. These two very different methods do not compete but rather supplement each other. PFA allows one easier and independently to vary different material properties and can be scaled up for much larger sample and longer process time than MD. MD provides atomistic mechanisms and can be easier applicable to simultaneous occurring of several processes (such as PT, plastic flow and fracture), provided that adequate interatomic potential is found.

Obtained results represent a closure of the multiscale problem of predicting the PT initiation conditions for real (defective) materials starting with atomistic simulations, development of PFA for an ideal crystal, and solving PFA problem for crystal with defect. They will be generalized for the case of multiple dislocations of different configuration. Also, there are current PFA efforts [4,9,10,28] to explain the strong reduction of the PT pressure by application of plastic shear [4,29–32], by factor of 10 [29] to as much as 100 [32]. This reduction is rationalized by considering the nucleation at the dislocation pileups produced by plastic shear but for a model material and 2D simulations. These problems should be solved in the 3D formulation for specific materials with well-defined lattice instability conditions.

Acknowledgement

The supports of NSF (CMMI-1536925 and DMR-1904830), ARO (W911NF-17-1-0225), ONR (N00014-19-1-2082), and Iowa State University (Vance Coffman Faculty Chair Professorship) are gratefully acknowledged. The simulations were performed at Extreme Science and Engineering Discovery Environment (XSEDE), allocations TG-MSS140033 and MSS170015.

Appendix

A System of equations

The formulations in this work are based on the general advanced PFA developed in Ref. [11], which was specified for cubic-to-tetragonal Si I↔Si II PTs in Ref. [15]. Here, we slightly advance the kinematics by taking into account the plastic deformation due to a single static dislocation.

A.1 Kinematics of combined phase transformation and dislocation

Multiplicative decomposition of the deformation gradient $\boldsymbol{F} = \frac{\partial \boldsymbol{r}}{\partial \boldsymbol{r}_0} = \nabla_0 \boldsymbol{r}$ into elastic $\boldsymbol{F}_e$, transformation $\boldsymbol{U}_t$, and plastic $\boldsymbol{F}_p$ parts reads to

$$\boldsymbol{F} = \boldsymbol{F}_e \cdot \boldsymbol{U}_t \cdot \boldsymbol{F}_p. \tag{2}$$

The Jacobian determinants describing the ratio of volumes and mass densities in the corresponding configurations are

$$J = \frac{dV}{dV_0} = \frac{\rho_0}{\rho} = det\boldsymbol{F};\ \ J_e = \frac{dV}{dV_t} = \frac{\rho_t}{\rho_0} = det\boldsymbol{F}_e;$$
$$J_{tp} = \frac{dV_t}{dV_p} = \frac{\rho_p}{\rho_t} = det\boldsymbol{U}_t det\boldsymbol{F}_p = det\boldsymbol{U}_t = J_t;\ \ J_p = det\boldsymbol{F}_p = 1;\ \ J = J_e J_t, \tag{3}$$

where $V_0(\rho_0), V_t(\rho_t), V_p(\rho_p)$, and $V(\rho)$ are the volumes (mass densities) in the reference Ω_0, intermediate Ω_t (after elastic unloading), intermediate Ω_p (after elastic unloading and reverse PT), and actual Ω configurations, respectively.

The Lagrangian total, elastic, transformation, and plastic strains are respectively given by

$$\boldsymbol{E} = \frac{1}{2}\left(\boldsymbol{F}^T \cdot \boldsymbol{F} - \boldsymbol{I}\right);\quad \boldsymbol{E}_e = \frac{1}{2}\left(\boldsymbol{F}_e^T \cdot \boldsymbol{F}_e - \boldsymbol{I}\right);\quad \boldsymbol{E}_t = \frac{1}{2}(\boldsymbol{U}_t \cdot \boldsymbol{U}_t - \boldsymbol{I});$$
$$\boldsymbol{E}_p = \frac{1}{2}\left(\boldsymbol{F}_p^T \cdot \boldsymbol{F}_p - \boldsymbol{I}\right); \boldsymbol{E} = \boldsymbol{F}_p^T \cdot \boldsymbol{U}_t \cdot \boldsymbol{E}_e \cdot \boldsymbol{U}_t \cdot \boldsymbol{F}_p + \boldsymbol{F}_p^T \cdot \boldsymbol{E}_t \cdot \boldsymbol{F}_p + \boldsymbol{E}_p \tag{4}$$

Phase transformation is described by the order parameter η with $\eta = 0$ for P_0 and $\eta = 1$ for P_1. The transformation deformation gradient is expressed as

$$\boldsymbol{U}_t(\eta) = \boldsymbol{I} + \boldsymbol{\varepsilon}_t \circ \boldsymbol{\varphi}(\boldsymbol{a}_\varepsilon, \boldsymbol{w}_\varepsilon, \eta);$$
$$\boldsymbol{\varphi} := \boldsymbol{a}_\varepsilon \eta^2 + (10\boldsymbol{\iota} - 3\boldsymbol{a}_\varepsilon + \boldsymbol{w}_\varepsilon)\eta^3 + (3\boldsymbol{a}_\varepsilon - 2\boldsymbol{w}_\varepsilon - 15\boldsymbol{\iota})\eta^4 + (6\boldsymbol{\iota} - \boldsymbol{a}_\varepsilon + \boldsymbol{w}_\varepsilon)\eta^5, \tag{5}$$

where $\boldsymbol{\varepsilon}_t = \boldsymbol{U}_t(1) - \boldsymbol{I}$ is the transformation strain after complete transformation from the parent phase P_0 to the product phase P_1; $\boldsymbol{\varphi}$ (and consequently, $\boldsymbol{a}_\varepsilon, \boldsymbol{w}_\varepsilon, \boldsymbol{\iota}$) are matrices (not second-rank tensors), which have the same non-zero components and symmetry as $\boldsymbol{\varepsilon}_t$ in the coordinate system of crystal lattice of P_0; all non-zero components of matrix $\boldsymbol{\iota}$ are equal to one. The Hadamard product is defined

as $\boldsymbol{\varepsilon}_t \circ \boldsymbol{\varphi} := \{\varepsilon_t^{ij}\varphi^{ij}\}$ with no summation over i and j. For cubic-to-tetragonal PT, the diagonal terms of transformation strain and all matrices are nonzero only, and two of three terms are the same for all matrices.

Considering a single slip system on a slip plane with the unit normal $\boldsymbol{k}$ and with the Burgers vector $\boldsymbol{b}$, the plastic deformation gradient $\boldsymbol{F}_p$ representing a simple shear is

$$\boldsymbol{F}_p = \boldsymbol{I} + \frac{1}{H}\boldsymbol{b}\otimes\boldsymbol{k} = \boldsymbol{I} + \gamma\boldsymbol{m}\otimes\boldsymbol{k}, \tag{6}$$

where $\gamma = \frac{|\boldsymbol{b}|}{H}$ is the plastic shear strain of the single dislocation in a dislocation band of the height H; $\boldsymbol{m}$ is the unit vector in the direction of $\boldsymbol{b}$. Parameters $\boldsymbol{k}$, $\boldsymbol{b}$ and H are determined in the reference configuration. It should be noted that the plastic deformation gradient leads to deformation only inside the dislocation band and there is no plastic deformation outside of the dislocation band (i.e., $\boldsymbol{F}_p = \boldsymbol{I}$).

A.2 Helmholtz free energy

We accept the expression for the Helmholtz free energy per unit reference volume as

$$\overline{\psi}(\boldsymbol{F}, \eta, \theta, \nabla_0\eta) = J_t\psi^e + \psi^\theta + \psi^\nabla, \tag{7}$$

where ψ^e is the elastic energy per unit volume in the intermediate configuration Ω_t, which is the reference configuration for the elasticity rule; ψ^θ is the thermal energy, which includes the double-well barrier between phases as well as the thermal driving force for phase transformation; and ψ^∇ is the gradient energy which penalizes interfaces.

A quadratic elastic energy for an orthotropic is considered [33].

$$\begin{aligned}\psi^e &= \frac{1}{2}\boldsymbol{E}_e : \boldsymbol{C} : \boldsymbol{E}_e = \frac{1}{2}C^{ijkl}E_e^{ij}E_e^{kl} \\ &= \frac{1}{2}\sum_{n=1}^{3}\left[\lambda^n\left(E_e^{nn}\right)^2 + 2\mu^n E_e^{nn}E_e^{kk} + 4\nu^n E_e^{nk}E_e^{kn}\right].\end{aligned} \tag{8}$$

The components of the fourth-rank elastic moduli tensor $\boldsymbol{C}$ are expressed as

$$\begin{aligned}C^{ijkl} = \sum_{n=1}^{3}\Big[&\lambda^n\delta^{in}\delta^{jn}\delta^{kn}\delta^{ln} + \mu^n\left(\delta^{in}\delta^{jn}\delta^{kl} + \delta^{ij}\delta^{kn}\delta^{ln}\right) \\ &+\nu^n\left(\delta^{in}\delta^{jk}\delta^{ln} + \delta^{jn}\delta^{ik}\delta^{ln} + \delta^{in}\delta^{jl}\delta^{kn} + \delta^{jn}\delta^{il}\delta^{kn}\right)\Big],\end{aligned} \tag{9}$$

where λ^n, μ^n, and ν^n are nine independent elastic constants, with three for each of the three orthogonal directions. For materials with a tetragonal crystal lattice, the constants for $n = 2$ and 3 are the same; for cubic lattices, constants for all n are the same; see Ref. [15] for explicit expressions of elastic constants. The constants λ^n, μ^n and ν^n are interpolated during the PT as

$$\begin{aligned}&\lambda^n = \lambda_0^n + (\lambda_1^n - \lambda_0^n)\varphi_e(\eta); \quad \mu^n = \mu_0^n + (\mu_1^n - \mu_0^n)\varphi_e(\eta); \\ &\nu^n = \nu_0^n + (\nu_1^n - \nu_0^n)\varphi_e(\eta),\end{aligned} \tag{10}$$

with λ_0^n, μ_0^n, ν_0^n and λ_1^n, μ_1^n, ν_1^n being the elastic constants of P_0 and P_1, respectively. The corresponding interpolation function is [11]:

$$\varphi_e(\eta) = \eta^3\left(10 - 15\eta + 6\eta^2\right). \tag{11}$$

The thermal part of the free energy can be expressed as

$$\psi^\theta = A\eta^2(1-\eta)^2 + \Delta\psi^\theta\left(3\eta^2 - 2\eta^3\right), \tag{12}$$

where A is the double-well barrier between P_0 and P_1 and $\Delta\psi^\theta$ is the difference between the thermal free energy of P_0 and P_1.

The gradient part of the free energy is presented in a standard form:

$$\psi^\nabla = \frac{\beta}{2}|\nabla_0\eta|^2, \tag{13}$$

where β is the gradient energy coefficient.

A.3 The first Piola-Kirchhoff and Cauchy stress tensors

The first Piola-Kirchhof stress and the Cauchy stress have the following expressions [11]:

$$\begin{aligned}&\boldsymbol{P} = \rho_0 J_t\boldsymbol{F}_e\cdot\frac{\partial\psi^e}{\partial\boldsymbol{E}_e}\cdot\boldsymbol{U}_t^{-1}\cdot\boldsymbol{F}_p^{T-1} = J_t\boldsymbol{F}_e\cdot\boldsymbol{C} : \boldsymbol{E}_e\cdot\boldsymbol{U}_t^{-1}\cdot\boldsymbol{F}_p^{T-1}; \\ &\boldsymbol{\sigma} = J^{-1}\boldsymbol{P}\cdot\boldsymbol{F}^T = \rho J_t\boldsymbol{F}_e\cdot\frac{\partial\psi^e}{\partial\boldsymbol{E}_e}\cdot\boldsymbol{F}_e^T = J_e^{-1}\boldsymbol{F}_e\cdot\boldsymbol{C} : \boldsymbol{E}_e\cdot\boldsymbol{F}_e^T.\end{aligned} \tag{14}$$

A.4 Ginzburg-Landau equation

The evolution of the order parameter and corresponding martensitic nanostructure can be described by the Ginzburg-Landau equation, which represents a linear relationship between the rate of change of the order parameter, $\dot{\eta}$, and the conjugate generalized thermodynamic force, X:

$$\dot{\eta} = LX = L\left(-\frac{\partial\overline{\psi}}{\partial\eta}\Big|_{\boldsymbol{E}} + \nabla_0\cdot\left(\frac{\partial\overline{\psi}}{\partial\nabla_0\eta}\right)\right), \tag{15}$$

where $L > 0$. is the kinetic coefficient. Substituting the free energy Eq. (7) into Eq. (15) results in the more explicit but still compact form of the Ginzburg-Landau equation in the reference configuration

$$\begin{aligned}\dot{\eta} = LX = L\Big(&\boldsymbol{P}^T\cdot\boldsymbol{F}_e : \frac{\partial\boldsymbol{U}_t}{\partial\eta} - J_t\frac{\partial\psi^e}{\partial\eta}\Big|_{\boldsymbol{E}_e} - J_t\psi^e\boldsymbol{U}_t^{-1} \\ &: \frac{\partial\boldsymbol{U}_t}{\partial\eta} - \frac{\partial\psi^\theta}{\partial\eta} + \beta\nabla_0^2\eta\Big).\end{aligned} \tag{16}$$

A.5 Equilibrium equation in the reference configuration

$$\nabla_0\cdot\boldsymbol{P} = \boldsymbol{0}. \tag{17}$$

A.6 Boundary conditions for the order parameter

Assuming that the surface energy does change during the PT, one obtains boundary conditions for the evolution of the order parameter as

$$\boldsymbol{n}_0\cdot\nabla_0\eta = 0, \tag{18}$$

where $\boldsymbol{n}_0$ is the normal to the surface in Ω_0.

A.7 Calibration of crystal lattice instability criteria for Si I–Si II PTs with MD

As elaborated in Ref. [15], the crystal lattice instability conditions for cubic-to-tetragonal PTs can be presented as

$$P_0 \rightarrow P_1: \quad (\sigma_1+\sigma_2)\varepsilon_{t1}a_{\varepsilon 1}+\sigma_3\varepsilon_{t3}a_{\varepsilon 3} \geq \frac{1}{J_e}(A+3\Delta\psi^{\theta});$$
$$P_1 \rightarrow P_0: \quad (\sigma_1+\sigma_2)\frac{\varepsilon_{t1}w_{\varepsilon 1}}{1+\varepsilon_{t1}}+\frac{\sigma_3\varepsilon_{t3}w_{\varepsilon 3}}{1+\varepsilon_{t3}} \geq \frac{1}{J}(A-3\Delta\psi^{\theta}), \tag{19}$$

where the components of the transformation strain tensor are $\varepsilon_{t1}=\varepsilon_{t2}=0.1753$ and $\varepsilon_{t3}=-0.447$. The PFA parameters can be calibrated based on the results of MD simulations in Refs. [12,13], and in particular, equaling the PFA lattice instability criteria in Eq. (19) with that in Eq. (1). The calibrated parameters, including the jump in thermal energy $\Delta\psi^{\theta}=6.35$ *GPa*, interpolation constants $\boldsymbol{a}_{\varepsilon}$ and $\boldsymbol{w}_{\varepsilon}$ for transformation strain, double-well barrier magnitude A, and jump in thermal energy $\Delta\psi^{\theta}$ are (see Ref. [15] for more details)

if $-\sigma_3 \geq 6.23$ GPa →
$A=0.75$ GPa, $a_{\varepsilon 1}=3.31$, $a_{\varepsilon 3}=3.60$, $w_{\varepsilon 1}=-2.48$, $w_{\varepsilon 3}=-2.39$,
otherwise →
$A=-9.48$ GPa, $a_{\varepsilon 1}=1.10$, $a_{\varepsilon 3}=2.26$, $w_{\varepsilon 1}=-3.88$, $w_{\varepsilon 3}=-3.73$. (20)

References

[1] G.B. Olson, M. Cohen, A general mechanism of martensitic nucleation: Part I. General concepts and the FCC-HCP transformation, Metall. Trans. 7A (1976) 1897–1904.
[2] G.B. Olson, M. Cohen, in: F.R.N. Nabarro (Ed.), Dislocation Theory of Martensitic Transformations, Dislocations in Solids 7, 1986, pp. 297–407.
[3] A.A. Boulbitch, P. Toledano, Phase nucleation of elastic defects in crystals undergoing a phase transition, Phys. Rev. Lett. 81 (1998) 838.
[4] V.I. Levitas, High-pressure mechanochemistry: conceptual multiscale theory and interpretation of experiments, Phys. Rev. B 70 (2004) 184118.
[5] G.B. Olson, A.L. Roytburd, in: G.B. Olson, W.S. Owen (Eds.), Martensitic Nucleation, Martensite 9, 1995, pp. 149–174.
[6] A.C.E. Reid, G.B. Olson, B. Moran, Dislocations in nonlinear nonlocal media: martensitic embryo formation, Phase Transitions 69 (1998) 309–328.
[7] W. Zhang, Y.M. Jin, A.G. Khachaturyan, Three-dimensional phase field model of proper martensitic transformation, Acta Mater. 55 (2007) 565–574.
[8] Y.C. Xu, W.F. Rao, J.W. Morris, A.G. Khachaturyan, Nanoembryonic thermoelastic equilibrium and enhanced properties of defected pretransitional materials, NPJ Comput. Mater. 4 1 (2018) 58.
[9] V.I. Levitas, M. Javanbakht, Phase transformations in nanograin materials under high pressure and plastic shear: nanoscale mechanisms, Nanoscale 6 (2014) 162–166.
[10] M. Javanbakht, V.I. Levitas, Phase field simulations of plastic strain-induced phase transformations under high pressure and large shear, Phys. Rev. B 94 (2016) 214104.
[11] V.I. Levitas, Phase field approach for stress- and temperature-induced phase transformations that satisfies lattice instability conditions. Part I. General theory, Int. J. Plast. (2018) 164–185, 106 0749-6419.
[12] V.I. Levitas, H. Chen, L. Xiong, Triaxial-stress-induced homogeneous hysteresis-free first-order phase transformations with stable intermediate phases, Phys. Rev. Lett. 118 (2017a), 025701.
[13] V.I. Levitas, H. Chen, L. Xiong, Lattice instability during phase transformations under multiaxial stress: modified transformation work criterion, Phys. Rev. B 96 (2017b), 054118.
[14] N.A. Zarkevich, H. Chen, V.I. Levitas, D.D. Johnson, Lattice instability during solid-solid structural transformations under general applied stress tensor: example of Si I → Si II with metallization, Phys. Rev. Lett. 121 (2018) 165701.
[15] H. Babaei, V.I. Levitas, Phase-field approach for stress- and temperature-induced phase transformations that satisfies lattice instability conditions. Part 2. simulations of phase transformations Si I↔Si II, Int. J. Plast. (2018) 223–245, 107 0749-6419.
[16] K. Mizushima, S. Yip, E. Kaxiras, Ideal crystal stability and pressure-induced phase transition in silicon, Phys. Rev. B 50 (1994) 14952.
[17] K. Gáal-Nagy, M. Schmitt, P. Pavone, D. Strauch, Ab initio study of the high-pressure phase transition from the cubic diamond to the β-tin structure of Si, Comput. Mater. Sci. 22 (2001) 49–55.
[18] V. Domnich, D. Ge, Y. Gogotsi, Indentation induced phase transformations in semiconductors, in: Y. Gogotsi, V. Domnich (Eds.), High Pressure Surface Science and Engineering, Institute of Physics, Bristol and Philadelphia, 2004, pp. 381–442.
[19] A. Kailer, Y.G. Gogotsi, K.G. Nickel, Phase transformations of silicon caused by contact loading, J. Appl. Phys. 81 (1997) 3057–3063.
[20] H. Huang, J. Yan, New insights into phase transformations in single crystal silicon by controlled cyclic nanoindentation, Scr. Mater. 102 (2015) 35–38.
[21] I. Yonenaga, An overview of plasticity of Si crystals governed by dislocation motion, Eng. Fract. Mech. (2015) 468–479, 147 0013-7944.
[22] J.P. Hirth, J. Lothe, Theory of Dislocations, second ed., Wiley, New York, 1982.
[23] J. Godet, P. Hirel, S. Brochard, L. Pizzagalli, Evidence of two plastic regimes controlled by dislocation nucleation in silicon nanostructures, J. Appl. Phys. 105 (2009), 026104.
[24] K. Shima, S. Izumi, S. Sakai, Reaction pathway analysis for dislocation nucleation from a sharp corner in silicon: glide set versus shuffle set, J. Appl. Phys. 108 (2010), 063504.
[25] W. Bangerth, R. Hartmann, G. Kanschat, deal.II – a general purpose object oriented finite element library, ACM Trans. Math Software 33 (4) (2007) 1–27.
[26] R.G. Hennig, A. Wadehra, K.P. Driver, W.D. Parker, C.J. Umrigar, J.W. Wilkins, Phase transformation in Si from semiconducting diamond to metallic beta-Sn phase in QMC and DFT under hydrostatic and anisotropic stress, Phys. Rev. B 82 (2010), 014101.
[27] V.I. Levitas, D.I. Preston, D.W. Lee, Three-dimensional Landau theory for multivariant stress-induced martensitic phase transformations. III. Alternative potentials, critical nuclei, kink solutions, and dislocation theory, Phys. Rev. B 68 (2003) 134201.
[28] V.I. Levitas, S.E. Esfahani, I. Ghamarian, Scale-free modeling of coupled evolution of discrete dislocation bands and multivariant martensitic microstructure, Phys. Rev. Lett. 121 (2018) 205701.
[29] C. Ji, V.I. Levitas, H. Zhu, J. Chaudhuri, A. Marathe, Y. Ma, Shear-induced phase transition of nanocrystalline hexagonal boron nitride to wurtzitic structure at room temperature and lower pressure, Proc. Natl. Acad. Sci. U.S.A. 109 (2012) 19108–19112.
[30] V.D. Blank, E.I. Estrin, Phase Transitions in Solids under High Pressure, CRC Press, 2013.
[31] K. Edalati, Z. Horita, A review on high-pressure torsion (hpt) from 1935 to 1988, Mater. Sci. Eng. A 652 (2016) 325–352.
[32] Y. Gao, Y. Ma, Q. An, V.I. Levitas, Y. Zhang, B. Feng, J. Chaudhuri, W.A. Goddard III, Shear driven formation of nano-diamonds at sub-gigapascals and 300 K, Carbon 146 (2019) 364–368.
[33] S.G. Lekhnitskii, Theory of Elasticity of an Anisotropic Elastic Body, Holden-Day Inc., 1963.